Available online at www.sciencedirect.com

ScienceDirect

Electrochimica Acta 53 (2008) 3084–3093

ELECTROCHIMICA Acta

www.elsevier.com/locate/electacta

Doping effects on structure and electrode performance of K-birnessite-type manganese dioxides for rechargeable lithium battery

A. Ogata[a], S. Komaba[a,*], R. Baddour-Hadjean[b], J.-P. Pereira-Ramos[b], N. Kumagai[c]

[a] *Department of Applied Chemistry, Faculty of Science, Tokyo University of Science, 1-3 Kagurazaka, Shinjuku, Tokyo 162-8601, Japan*
[b] *Institut de Chimie et des Matériaux Paris Est, CNRS-UMR 7182, GESMAT 2 rue Henri-Dunant, 94320 Thiais, France*
[c] *Department of Frontier Materials and Functional Engineering, Graduate School of Engineering, Iwate University, Iwate 020-8551, Japan*

Received 25 September 2007; received in revised form 6 November 2007; accepted 11 November 2007
Available online 22 November 2007

Abstract

The potassium birnessites doped with Al, Ni, and Co were prepared by calcination and aqueous treatment, which showed that single phase products were obtained with Ni and Al up to 5 at.% and Co up to 25 at.% addition to strating $KMnO_4$. The discharge–recharge capacities and capacity retentions in an aprotic Li cell were not improved by the Ni and Al dopings, but those of the cobalt doped birnessite were improved. The initial discharge capacities of the undoped and cobalt doped birnessites were 170 and 200 mAh g^{-1} with capacity retentions of 56 and 80% during the initial 20 cycles, respectively. The reasons for the improvement of the battery performance by Co doping were considered as follows: (i) a change in the stacking structure, (ii) a decrease in the charge transfer resistance, and (iii) improved structural stability of the oxide. Their micro structures were evaluated by X-ray diffraction, photoelectron and Raman spectroscopies, and electron microscopy. Also, potassium birnessite synthesized by adding about 3 times excess potassium indicated that the stacking structure was similar to the 30 at.% cobalt doping sample, furthermore, the better capacity retention was achieved as cathode in a Li cell.

Keywords: Birnessite; Manganese dioxide; Lithium intercalation; Lithium battery; Positive electrode

1. Introduction

Manganese oxides have been studied for electrochemical energy storage due to being a low toxic and inexpensive material which form lamellar, spinel and tunnel frameworks [1–3]. The electrochemically active materials, which have a working potential for Li insertion/deinsertion around 3–4 V vs. Li, are strong candidates for lithium (ion) batteries. As one of the manganese oxides, the birnessite-type manganese oxide is a hydration-layered manganese oxide, which forms MnO_2 sheets of MnO_6 octahedra assembled in layers and has cations of pillar (mainly alkaline ion) and lattice water in the interlayer space. Up to now, the syntheses of the birnessite are achieved by various methods such as a calcination reaction [4–12], sol–gel synthesis [12–15], hydrothermal synthesis [16,17], etc. The structural details of potassium-containing birnessite were investigated as previously reported [4–8]. These materials show a working potential around 3 V vs. Li and high discharge capacities during initial cycling, though there is the problem of structural collapse resulting in discharge capacity fading [5,15]. In order to improve the battery performance, Franger et al. [15] and Tsuda et al. [13] reported the enhancement of the cycle performance by Co doping in birnessite.

Previously, we reported the synthesis of a birnessite by utilizing the thermal decomposition of $KMnO_4$ and its electrochemical performance in Li cells [9,10]. In the present paper, we report that potassium birnessites made by thermal decomposition reaction of $KMnO_4$ mixed with Co, Ni, Al, Mn, and K nitrates, and we investigated the relation between the synthetic conditions and electrochemical performance.

2. Experimental

The layered manganese dioxides doped with Al, Ni, or Co were obtained by the calcinations of mixtures (about 0.5 g) of $KMnO_4$ and Al, Ni, or Co nitrate, respectively, which were dissolved in several ml of distilled water, at 600 °C (50 °C h^{-1}) for 5 h in air. The calcined sample was ultrasonically treated

---

[*] Corresponding author. Tel.: +81 3 5228 8749; fax: +81 3 5228 8749.
E-mail address: komaba@rs.kagu.tus.ac.jp (S. Komaba).

0013-4686/$ – see front matter © 2007 Elsevier Ltd. All rights reserved.
doi:10.1016/j.electacta.2007.11.038

for 5 min in a sufficient amount of water. The precipitate in the ultrasonically treated solution was then separated by filtration, washed with water until neutral, and dried at 80 °C for 24 h in air. We synthesized the samples using metal nitrate addition with the molar ratios Me/(Me + Mn) (Me = Al, Ni, and Co) of 0, 0.05, 0.15, 0.25 and 0.50 in strating materials, and these samples were hereafter defined as undoped, Me-5, Me-15, Me-25 and Me-50, respectively.

$KMnO_4$ powder was mixed with manganese or potassium nitrate at the molar ratios of K/Mn = 1/3, 1/2, 1 (pure $KMnO_4$), 2, 3, 5, or 10, and we called the calcined samples as Mn-3, Mn-2, undoped, K-2, K-3, K-5, and K-10, respectively. These calcined samples were obtained under the same calcination conditions and ultrasonically treated in water, filtered and dried.

The phase identification of the products was carried out by powder X-ray diffractometry (XRD) using Cu Kα radiation. The composition of K, Mn and Co in the products was determined by atomic absorption spectrometry (AAS) after dissolving the products in HCl and/or H_2O_2 aqueous solutions. Water content was measured from weight loss by heating at 300 °C. The morphology of the products was observed by transmission electron microscopy (TEM). The valences of the Mn and Co in the products were evaluated by X-ray photoelectron spectroscopy (XPS). The thermal behavior of the starting mixture and obtained samples was examined by thermogravimetry (TG) at 10 °C min^{-1}. Raman scattering (RS) spectra were taken between 140 and 1000 cm^{-1} at room temperature in a backscattering configuration. A confocal Labram HR 800 (HORIBA JobinYvon) spectrometer combined with an open microscope and a X,Y Piezoelectric stage to position the sample with the best accuracy and repeatability was used. The laser light source was the 514.5 nm line radiation from an Argon ion (514.5 nm) laser. The scattered light is collected by the objective in a confocal geometry, and is dispersed onto an air cooled CCD array by a 1800 lines/mm grating. The investigated area is in the order of 1 μm^2. The frequency stability and the accuracy of the apparatus were checked recording the Raman spectrum of silicon. To avoid sample photodecomposition or damaging, RS spectra were recorded using a low excitation power of 20 μW, an increase in lattice temperature generally resulting in a shift of Raman peak wavenumbers up to the formation of Mn_3O_4 oxide. A decomposition of the spectra within the limits 300 and 800 cm^{-1} was performed with the LABSPEC® automatic fitting software provided with the spectrometer.

For the electrochemical measurements, the positive electrode mixtures consisted of manganese oxide, graphite, acetylene black as the conductive agent, and poly(vinylidene fluoride) as the binder in the weight ratio of 7:1:1:1. Lithium foil was used for the counter electrodes. The electrolyte was 1 mol dm^{-3} $LiClO_4$-propylene carbonate (PC). The discharge–recharge tests were carried out between 2.0 and 4.3 V vs. Li/Li^+ at 20 mA g^{-1}. The alternating current (AC) impedance measurement before and after the initial discharge was carried out in the frequency region between 1 mHz and 100 kHz, and the AC amplitude was 10 mV. Cells were stored for 24 h at open circuit prior to these measurements.

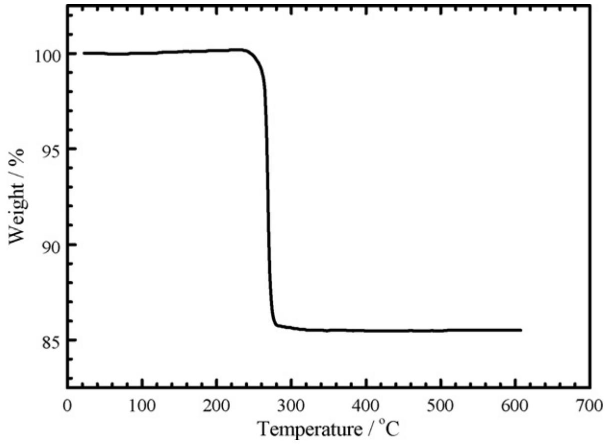

Fig. 1. TG curve of thermal decomposition reaction of $KMnO_4$ between room temperature to 600 °C at 10 °C min^{-1}.

3. Results and discussion

Fig. 1 shows the TG curve of the $KMnO_4$ powder. Below 230 °C, the weight of $KMnO_4$ is constant. At temperatures higher than 230 °C, the weight quickly decreased to 85.5%, and then the weight did not change up to 600 °C. The weight loss around 250 °C is due to the thermal decomposition of $KMnO_4$ as previously reported [11]. The weight loss is expressed by the following equation.

$$5KMnO_4 \rightarrow 3MnO_2 + K_2MnO_4 + K_3MnO_4 + 3O_2$$

Based on this thermal decomposition, the weight loss due to the O_2 evolution is estimated to be about 12 wt% which corresponds to the experimental weight loss around 250 °C. Therefore, it indicated the formation of an MnO_2 product and potassium manganates at >300 °C. Since these potassium manganates were removed from the sample after ultrasonically treating with water, we obtained the single phase of a layered MnO_2, at that time, potassium ions and water molecules were incorporated in an MnO_2 product, resulting in $K_xMnO_2 \cdot nH_2O$. Previously, we reported that the K-birnessite-type manganese oxide obtained by calcination at 600 °C and washing with water indicated better battery performance [9,10].

3.1. Doping with Al, Ni, and Co

The XRD patterns of the synthesized products from mixtures of $KMnO_4$ and the Al, Ni, or Co nitrates at 600 °C are shown in Fig. 2. Although the single phase of birnessite was obtained by the thermal decomposition of pure $KMnO_4$, the products depended on the addition of the nitrates.

Fig. 2 confirmed that a single phase was produced when Co nitrate was added up to 25%. The Co-50, which contained Co_3O_4 as an impurity, was formed. The Al-5 and Ni-5 samples were a single phase of birnessite. For the Al-15 and Al-25 samples, there appeared diffraction peaks of birnessite with several unindexed peaks, indicating that a single phase was not obtained. From the diffraction patterns of Ni-15 and Ni-25, the birnessite appeared together with NiO as an impurity. These results

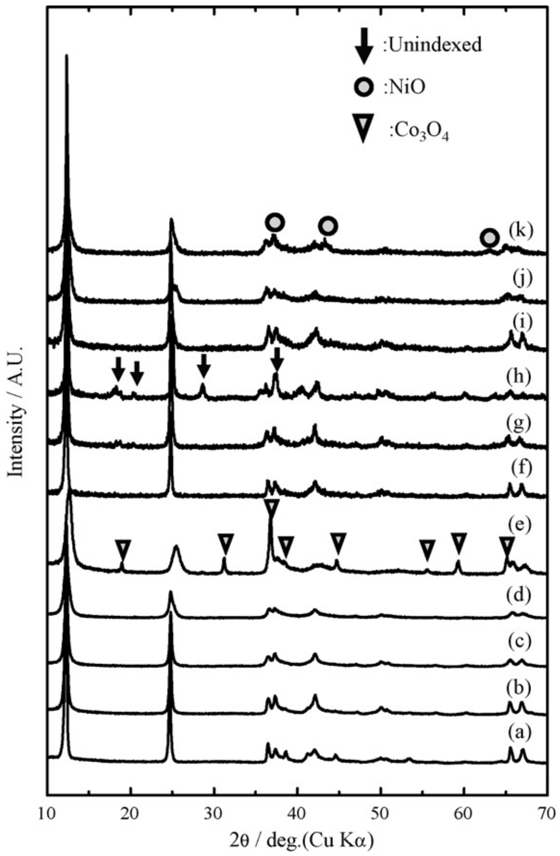

Fig. 2. XRD patterns of synthesized samples, (a) undoped, (b) Co-5, (c) Co-15, (d) Co-25, (e) Co-50, (f) Al-5, (g) Al-15, (h) Al-25, (i) Ni-5, (j) Ni-15, and (k) Ni-25. The symbols of (↓), (◯) and (▼) indicate unindexed, NiO and Co_3O_4 diffraction peaks, respectively.

reveal that the single phase products of birnessite were obtained for undoped, Co-5, Co-15, Co-25, Al-5, and Ni-5, and their *d* values of $0\,0\,l$ at $2\theta = $ ca. 12° are 7.22, 7.18, 7.18, 7.17, 7.19, and 7.08 Å, respectively. We believe that these birnessites were doped with definite amounts of Co, Al, and Ni.

Fig. 3 shows the discharge–recharge curves of the single phase birnessite products of the undoped and doped with Ni, Al, and Co. All the birnessite electrodes indicated S-shaped curve characteristics of the layer structure around 3 V. The undoped product showed the typical discharge–recharge behavior of Li de-/intercalation from/into the birnessite-type MnO_2 [4,5,9–17]. The shapes of the discharge–recharge curves hardly depended upon the doping with Al, Ni, and Co, suggesting that the Li intercalation into birnessite was not remarkably affected by the doping. On the other hand, when we compared the maximum discharge capacities, the capacity of the undoped is about 170 mAh g^{-1} whereas lower capacities of Al and Ni and a higher capacity of Co were obtained. For Ni-5 and Al-5, the obtained capacity was about 160 mAh g^{-1}. However, the higher capacity of ca. 190 mAh g^{-1} was achieved for Co-5 when compared to that of the undoped one. During the successive cycles, the capacity retention depends on the doping as seen in Fig. 3. Also, the additional small plateau was observed around 4 V in discharge–recharge curves. The plateau would indicate the formation of the spinel Li–Mn–O phase, and the corresponding capacity at 4 V gradually increases during successive cycling. It is likely that the appearance of 4 V plateau was due to the phase transition from birnessite to spinel during Li intercalation/deintercalation, as observed for the other MnO_2 compounds [18].

Fig. 4 shows the relation between the discharge capacity of these birnessites and cycle number. The maximum discharge capacities were reached at the 2nd cycle, and then the capacities gradually decreased during the following cycles for all samples. After 20 cycles, the discharge capacities of the undoped, Al-5, and Ni-5 decreased from 172, 161, and 155 to 97, 86, and 96 mAh g^{-1}, respectively. Their capacity retention ratios were about 56–62%. The Co-doping improved not only the discharge capacity, but also the capacity retention, i.e., the second capacity of 193 mAh g^{-1} decreased to 134 mAh g^{-1} at the 20th cycle. Its capacity retention increased from 56 to 70% due to the Co-doping. We will discuss the details of the Co doped birnessite in the next section.

3.2. Improvement by Co doping

Fig. 5(I) shows the XRD patterns of the undoped and the Co-5, −15, and −25 products. All the diffraction peaks can be indexed as birnessite-type manganese oxides without any secondary phase peaks, that is, no impurity phase, and the single phase of birnessite was prepared by calcining mixtures of $KMnO_4$ and Co nitrate. Their *d* values of $0\,0\,l$ around $2\theta = $ ca. 12° of undoped, Co-5, Co-15, and Co-25 are 7.22, 7.18, 7.18, and 7.17 Å, respectively, revealing that the *d* values were gradually decreased by Co doping. The decrease of the *d* value might be due to the change of stacking structure between 2H and 3R [6–8] and/or the substitution of the smaller ion of Co^{3+} (0.63 Å) for larger ion of Mn^{3+}(0.68 Å) as described below in Fig. 7. These XRD patterns of the samples showed that the diffraction peaks between 35° and 70° are different. In previous reports [6–9], several stacking phases are known to be formed as the birnessite-type manganese dioxides, such as the 2H phase (hexagonal unit cell and two layer periodicity, space group: $P6_3/mmc$) and 3R phase (rhombohedral unit cell and three layer periodicity, space group: $R\text{-}3m$), etc. The different stacking model of the 2H and 3R phases is schematically shown in Fig. 6. The stacking structures of these samples were able to be assigned to the mixtures of the 2H and 3R stacking phases from the XRD patterns in Fig. 5(I). Fig. 5(II) shows the variation of the 2H and 3R phases by the bar graph, which represented the fluctuations of the stacking phases. Based on the relative intensity of the XRD profile, the ratios of the 3R stacking phase to the 2H stacking phase are changed by Co doping, which were observed by the increased 3R stacking structure and decreased 2H stacking structure due to the increase in the Co doping.

The chemical compositions of the undoped and Co doped birnessites are shown in Table 1 by assuming no oxygen deficiency. From the table, when the starting Co mole ratio increased up to 0.25, the final Co mole ratio in the resultant birnessite increased to 0.30. And, the amount of the potassium constituent in birnessite did not significantly change between 0.2 and 0.3, which is not very different among the four birnessites. Based

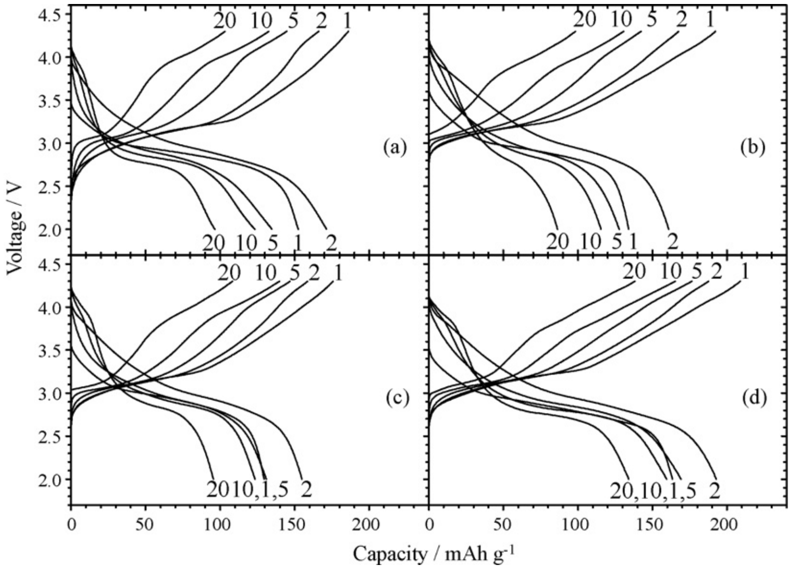

Fig. 3. Discharge–recharge curves of undoped and Me-doped products, (a) undoped, (b) Al-5, (c) Ni-5, and (d) Co-5. Current density is 20 mA g^{-1}.

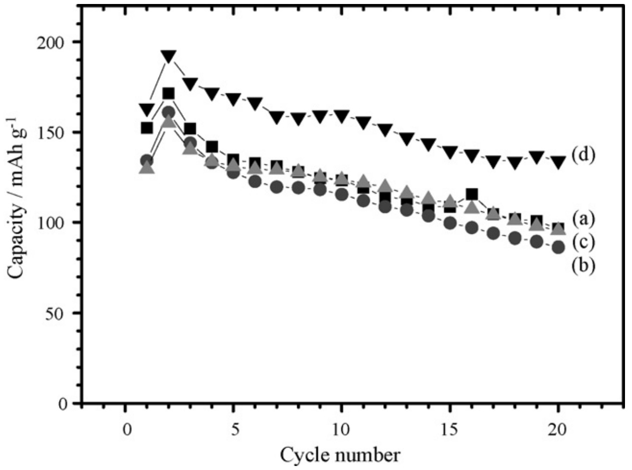

Fig. 4. Variation in discharge capacity of (a) undoped, (b) Al-5, (c) Ni-5, and (d) Co-5.

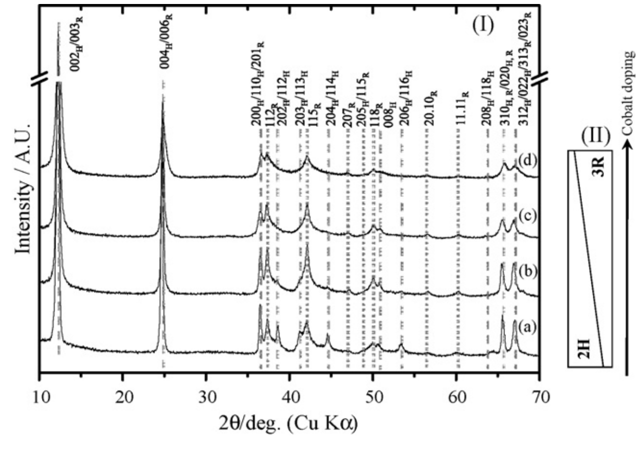

Fig. 5. (I) XRD patterns of (a) undoped ($K_{0.31}MnO_2{\cdot}0.37H_2O$), (b) Co-5 ($K_{0.21}Mn_{0.88}Co_{0.12}O_2{\cdot}0.41H_2O$), (c) Co-15 ($K_{0.21}Mn_{0.79}Co_{0.21}O_2{\cdot}0.37H_2O$), and (d) Co-25 ($K_{0.27}Mn_{0.70}Co_{0.30}O_2{\cdot}0.39H_2O$) products. The hkl_H and hlk_R of Millar Indexes indicate 2H stacking structure and 3R stacking structure, respectively. (II) The bar graph shows the ratio of the 2H and 3R phases.

on these results, we confirmed single phase birnessite doped with Co, when the mixture of $KMnO_4$ and Co nitrate was heat-treated at 600 °C. Because of the monotonous increase of y in $K_xMn_{1-y}Co_yO_2{\cdot}nH_2O$ from 0 to 0.30, furthermore, the increase in the amount of added Co nitrate produced a higher level of Co doping in birnessite, accompanied by a change in the stacking sequence from 2H to 3R.

In order to confirm the manganese and cobalt valences, XPS analyses were carried out. Fig. 7 shows the Mn 2p and Co 2p spectra of the products obtained for the undoped and Co doped birnessites. The Mn $2p_{3/2}$ peaks of the Mn(III) and (IV) chemical states appear around 641.4 and 642.4 eV [19]. Note that the ratio of the peak intensity of manganese 3+ decreased and the manganese 4+ increased with the increasing cobalt quantity. Therefore, the manganese average valences were increased by the cobalt ion doping in the structure. In general, the Co ion exists in the 2+ or 3+ oxidation states in the oxide formed at 600 °C in air. The binding energy of Co $2p_{3/2}$ at 780.3 eV probably indicates the presence of Co(III) [19]. As a result, the Mn valence states of the undoped and Co doped samples are 3 and 4+ coexist. Consequently, the Co(III) in birnessite was partially substituted for the Mn(III), and the cobalt ion partially occupied the Mn site.

Because it is sensitive to amorphous components and those with short-range order, Raman spectroscopy is very useful to study the structure of MnO_x materials, where crystalline disorder may be expected. Because Mn atoms in manganese dioxides are

Table 1
Chemical compositions of synthesized birnessites from mixtures of $KMnO_4$ and cobalt nitrate

Samples	Composition of products
Undoped	$K_{0.31}MnO_2{\cdot}0.37H_2O$
Co-5	$K_{0.21}Mn_{0.88}Co_{0.12}O_2{\cdot}0.41H_2O$
Co-15	$K_{0.21}Mn_{0.79}Co_{0.21}O_2{\cdot}0.37H_2O$
Co-25	$K_{0.27}Mn_{0.70}Co_{0.30}O_2{\cdot}0.39H_2O$

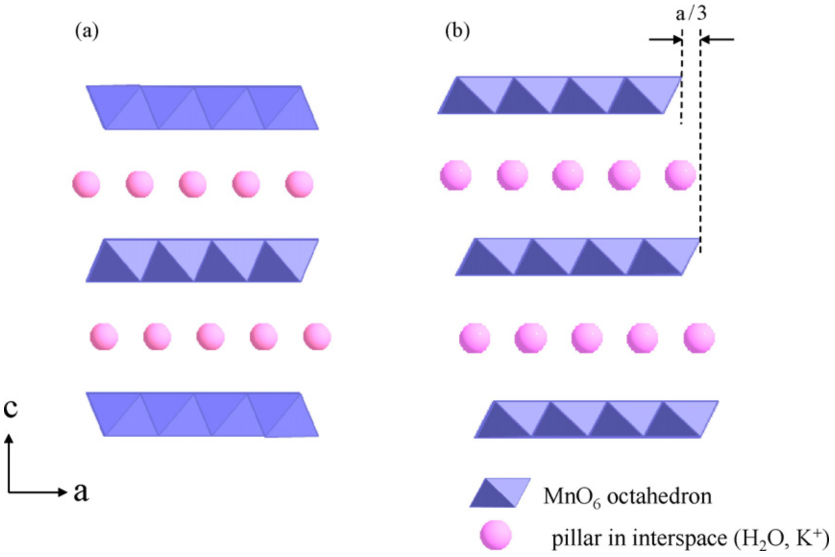

Fig. 6. The different stacking models of (a) 2H and (b) 3R phases.

always 6-fold coordinated, the Raman bands of MnO_2 materials depends on the MnO_6 octahedral environments (e.g. edge/corner sharing, Jahn–Teller distorsion, interactions with water/cations in the tunnels or layers of MnO_2 materials). Their Raman frequencies in the 500–700 and 200–500 cm^{-1} range have been assigned to the Mn–O stretching of MnO_6 octahedra and the Mn–O–Mn bending vibrations in the MnO_2 octahedral lattice, respectively [20].

Fig. 8 shows the Raman spectra of the undoped and Co-25 manganese oxides samples having the birnessite-type structure. The general peculiarity of the vibrational features of birnessite-type MnO_2 compounds is their low Raman activity. Three major features have been previously reported at 500–510, 575–585 and 625–650 cm^{-1} [14]. The two high-wavenumber bands are dominating all spectra, while bands in the low-frequency region appear with a rather weak intensity. According to the group theoretical calculation, manganese dioxide materials with monoclinic $C2/m$ space group ($Z=4$), i.e. C^3_{2h} spectroscopic symmetry, are predicted to show nine Raman-active modes with $3A_g + 6B_g$ species. Experimental results show that four components are always detected here, located at 409, 498, 575, and 638 cm^{-1} for the undoped sam-

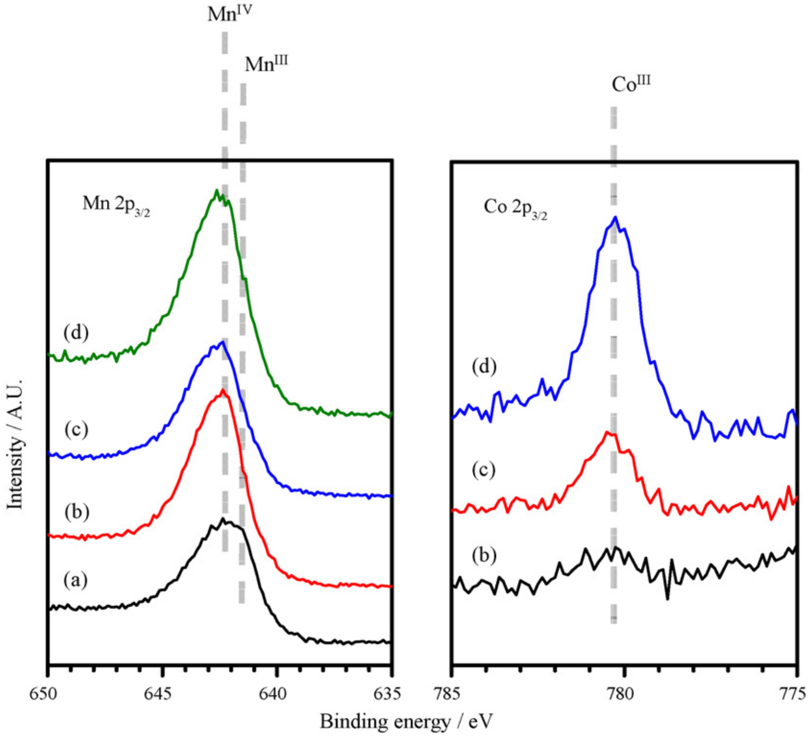

Fig. 7. Mn 2p and Co 2p XPS spectra of (a) undoped, (b) Co-5, (c) Co-15, and (d) Co-25 products.

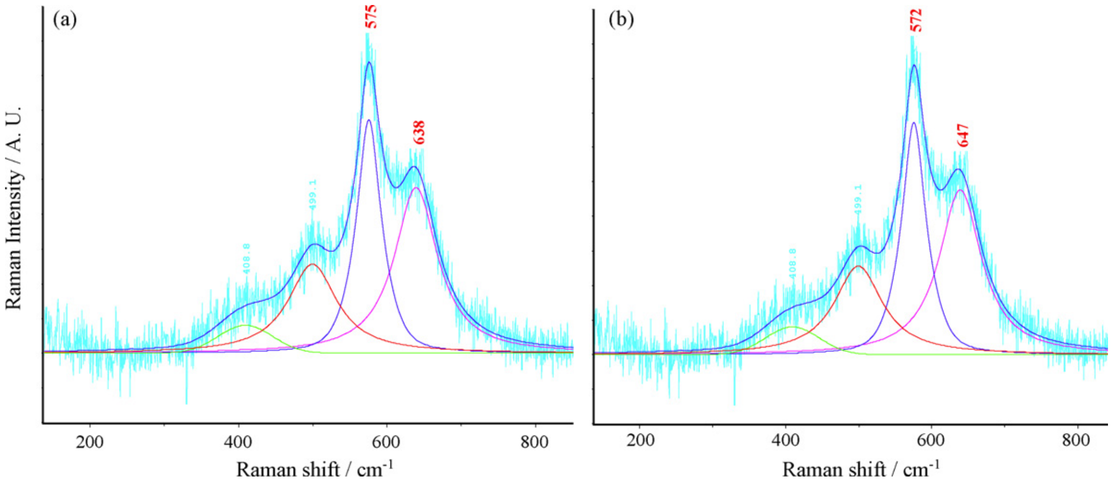

Fig. 8. Raman spectra of (a) undoped and (b) Co-25 samples.

ple, at 409, 498, 572 and 647 cm^{-1} for the doped Co-25 sample (Fig. 8).

These Raman features are very similar to those previously reported for several birnessite-type compounds [14]. The discrepancy between group factor analysis and Raman data is attributed to the defect chemistry and the local disorder of the birnessite structure. The presence of vacancies in the $[MnO_6]$ sheets of $MnO_2 \cdot nH_2O$ compounds breakdowns the crystal symmetry and lowers the spectroscopic symmetry. Therefore, Raman spectra of synthetic birnessites show variation in band position and, to a larger extent, relative band intensity.

The RS spectra of the Co-free sample support its proposed layered structure. The Raman band at 638 cm^{-1} can be viewed as the symmetric stretching vibration ν_2(Mn–O) of MnO_6 groups. It is assigned to the A_{1g} symmetric mode in the C_{2h}^3 spectroscopic space group. The band located at 575 cm^{-1} usually attributed to the ν_3(Mn–O) stretching vibration in the basal plane of $[MnO_6]$ sheets, is particularly strong in birnessite compounds, which can be related to the high rate of Mn(IV) in the birnessite family. The RS spectrum of the Co-25 sample, where cobalt partly substitutes for manganese, displays similar features than the Co-free sample. The most important Raman change is observed on the ν_2(Mn–O) stretching frequency, which presents a shift of 9 cm^{-1} towards the high-wavenumber side for the Co-doped sample. This result indicates a strengthening of the Mn–O bond along the interlayer direction in the Co-doped sample, as a consequence of the difference between ionic radii, i.e. $r(Mn^{3+}) = 0.68$ Å and $r(Co^{3+}) = 0.63$ Å. This result gives evidence for the effective partial replacement of Mn^{3+} by Co^{3+}, which induces a stronger network energy of the Co-doped material. We can recognize that the Mn^{3+} was partly replaced by Co^{3+}. Therefore, the results of Raman measurement correspond to the results of the XRD, XPS, and AAS measurements.

The TEM images of the undoped and Co-doped birnessites are displayed in Fig. 9. In this figure, regardless of the undoped and doped with Co in the birnessite, the crystallite sizes of these products are not very different. The particles of all the samples are plate-like crystals and the crystallite sizes are about 50–200 nm. It is considered that the difference in the particle sizes does not affect the discharge–recharge capacity and discharge capacity retention of the Li battery cathode materials. In order to examine the dependence of the amount of Co doping, we carried out galvanostatic discharge–recharge tests.

The discharge–recharge experiments of the undoped and Co-doped birnessite were performed at room temperature in the voltage range of 2.0–4.3 V by applying a current density of 20 mA g^{-1}. In Fig. 10, the discharge capacities of the undoped and Co-25 samples at the 2nd cycle indicated about 170 and 200 mAh g^{-1}, and the discharge reactions of these electrodes mainly progressed at 2.7–3.5 V. Though the redox capacity of $Mn^{3+/4+}$ couple in the birnessite usually decreased by cobalt doping as described in [15], surprisingly, the discharge capacities increased with the increasing Co quantity. The reasons for the increase of capacities should be due to the change in the 3R/2H stacking structure (Fig. 5) and higher electronic conductivity [21].

Fig. 11 shows the variation in the discharge capacities of the undoped and Co doped birnessites up to 20 cycles. The discharge capacities from the 2nd cycle to the 20th cycle of the undoped and Co-25 samples are changed from 170 to 95 mAh g^{-1} and from 200 to 160 mAh g^{-1}, respectively. Moreover, the discharge capacity retentions of the undoped and Co-25 birnessite are about 56 and 80% between 2nd and 20th cycles. The increases in the discharge capacity and the improvement of capacity retention by Co doping are probably due to improvement of the electro-conductivity [21] and the change of the ratio of stacking phase by the increase of 3R phase and decrease of 2H phase. It seems that the 3R stacking favors the reversible lithiation compared with the 2H one in structural points of view. Furthermore, the structure should be more stable during lithiation cycling since the shape of the discharge curves of the Co-25 (3R stacking phase) was almost preserved during 20 cycles whereas that of the undoped sample (2H stacking phase) was changed as seen in Fig. 10a and d. Additionally, the Co(III) valence state is more appropriate to stabilize the whole oxide against reversible lithiation than the Mn(III) valence state [13].

The Cole–Cole plots of the undoped and Co-25 products between before and after the first discharge reaction were shown

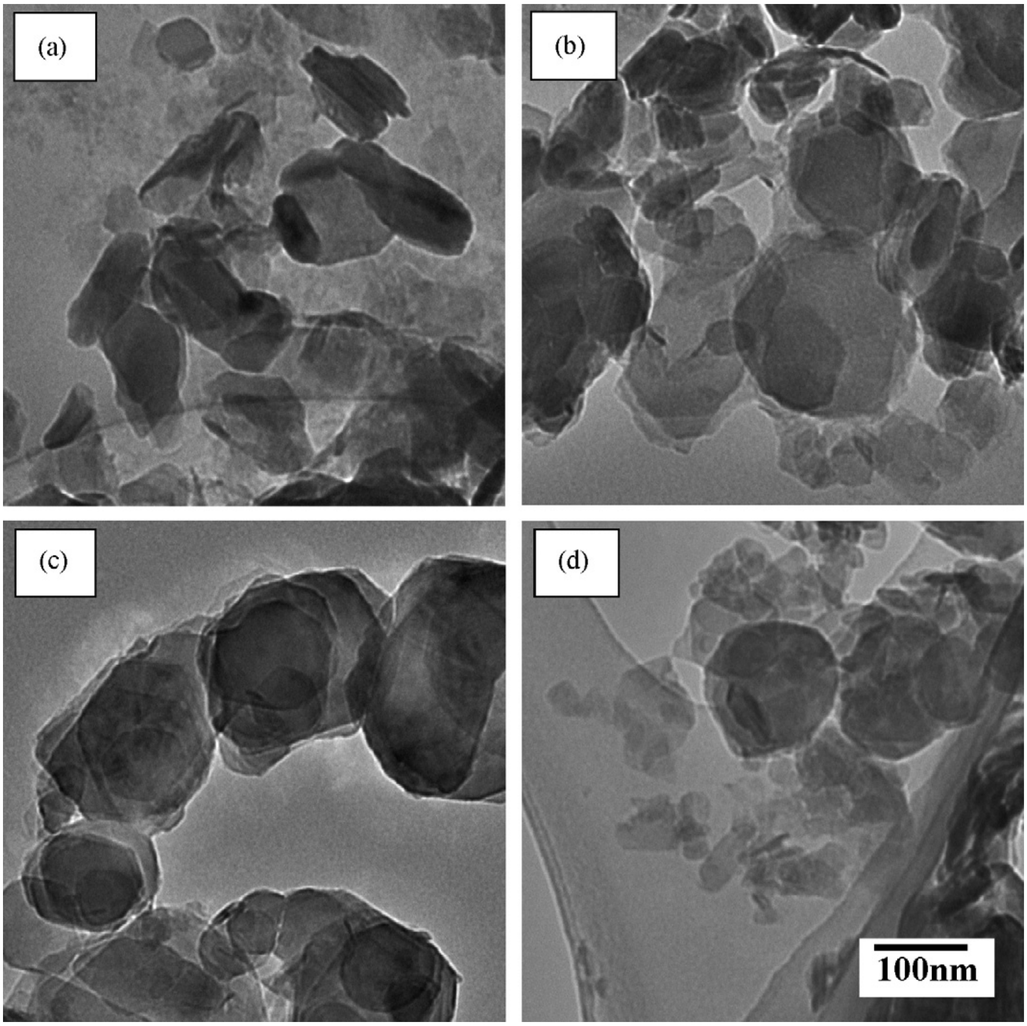

Fig. 9. TEM images of (a) undoped, (b) Co-5, (c) Co-15, and (d) Co-25 products.

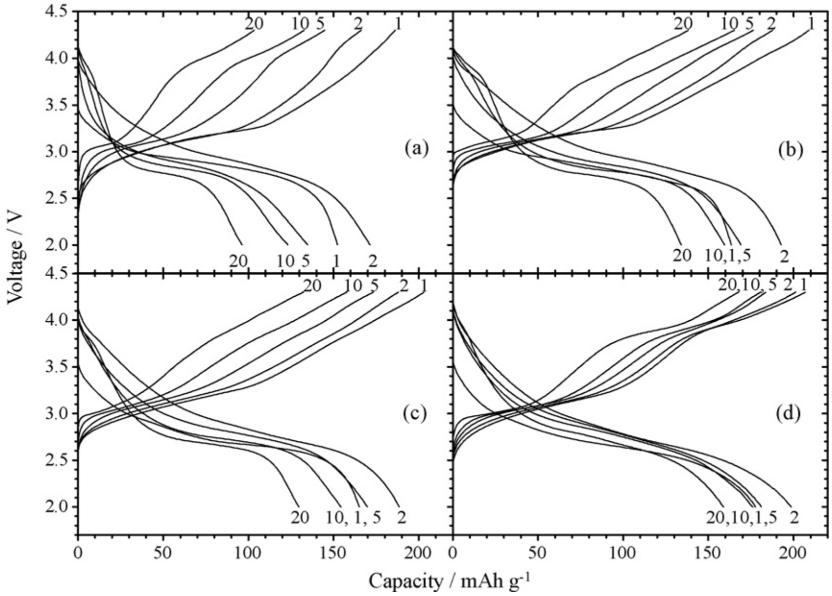

Fig. 10. Discharge–recharge curves of undoped and Co-doped birnessites, (a) undoped, (b) Co-5, (c) Co-15, and (d) Co-25. Current density is 20 mA g^{-1}.

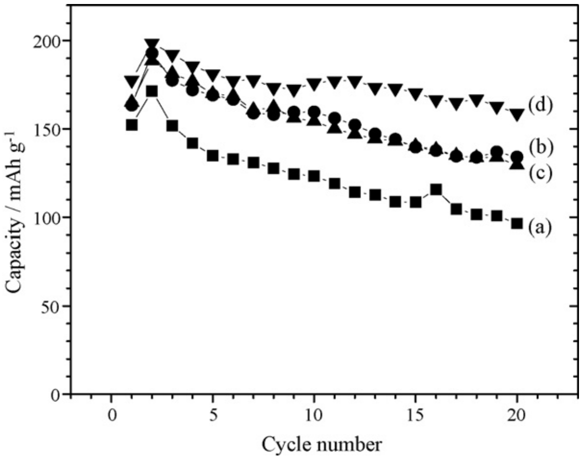

Fig. 11. Variation in discharge capacities of undoped and Co-doped birnessites, (a) undoped, (b) Co-5, (c) Co-15, and (d) Co-25.

in Fig. 12. In the initial state (before the first discharge), the semi-circles in the high-medium frequency range exhibit a charge transfer resistance [15], and the charge transfer resistance of Co-25 is apparently lower than the undoped product because the semi-circle is smaller than that of the undoped product. After the first discharge reaction, the resistance of the Co-25 product is lower than the undoped one, and the charge transfer resistances of both the undoped and Co-25 increased when comparing the Cole–Cole plots before and after. The resistance of the Co-25 product is always lower than that of the undoped one. Consequently, the K-birnessite doped with Co in its structure had a decreased charge transfer resistance which contributed to the increase in the discharge capacity.

3.3. Synthesis of K-birnessite by addition of excess K or Mn

As mentioned above, the addition of the cobalt nitrate led to the partial replacement of Mn site with cobalt. In the same manner, the dependence of K/Mn atomic ratio was investigated by adding potassium and manganese nitrates into $KMnO_4$. Fig. 13(I) shows the XRD patterns of the synthesized samples with the various mole ratios of K/Mn = 1/3, 1/2, 1 (undoped), 2, 3, 5, and 10 (in case of K/Mn = 1, pure $KMnO_4$ as the starting material). Fig. 13(II) indicates the phases of the prepared samples using a bar graph. The synthesized products of the Mn-3 and Mn-2 samples consisted of the coexisting birnessite and hollandite phase from these diffraction peaks. For the mole ratio of K/Mn = 1 or higher, all the diffraction peaks can be indexed as the birnessite phase in the XRD patterns, indicating birnessite without any secondary phases. And the *d* values of 0 0 *l* around 2θ = ca. 12° of undoped, K-2, K-3, K-5, and K-10 products are 7.22, 7.15, 7.17, 7.12, and 7.10 Å, respectively. The decrease of the *d* value might be suggestive of the change of stacking structure between 2H, 3R, and monoclinic phase [6–8]. From the AAS, the atomic ratios of K and Mn corresponded to around 0.25 in these birnessites (undoped and K-2, −3, −5, and −10), independent of the starting K/Mn values, though the XRD patterns of the undoped and K-2 to −10 are different between 35° and 70°. The ratios of the 2H and 3R stacking phases in these peaks depend on the amount of the potassium additives. Similar to those in Fig. 5, the decrease in the 2H stacking phase and increase in the 3R stacking phase were supported by these diffraction peaks. For K-10, the diffraction peaks, which are based on the 2H and 3R stacking phases, disappeared, and a

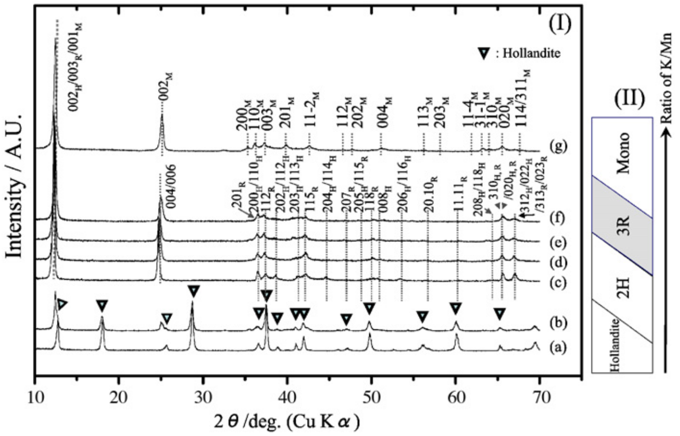

Fig. 13. (I) XRD patterns of synthesized samples with various mole ratios of K/Mn, (a) Mn-3, (b) Mn-2, (c) undoped, (d) K-2, (e) K-3, (f) K-5, and (g) K-10. (II) The bar graph shows the phase type of the prepared samples. The 2H, 3R, and Mono indicate 2-layer hexagonal, 3-layer rhombohedral, and monoclinic stacking phases, respectively.

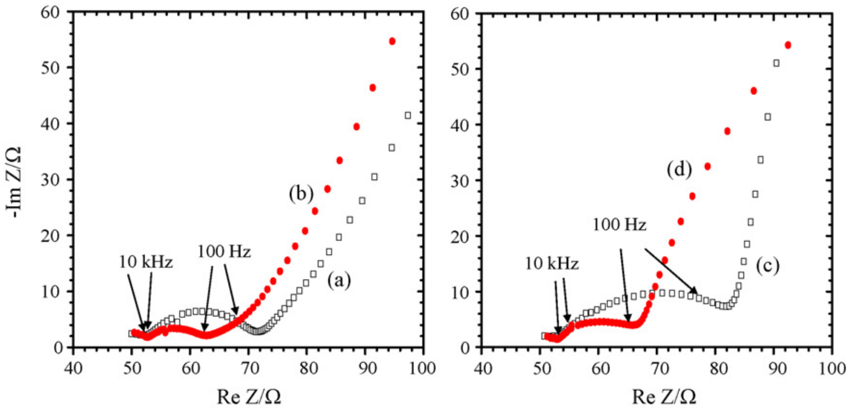

Fig. 12. Cole–Cole plots of (a) undoped and (b) Co-25 products before first discharge and (c) undoped and (d) Co-25 products after first discharge.

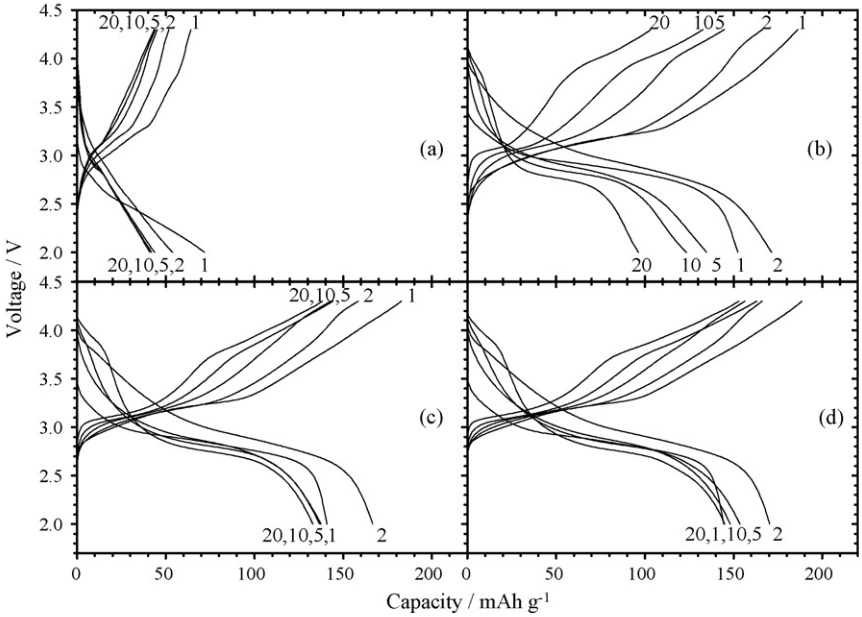

Fig. 14. Discharge–recharge curves of synthesized samples with various K/Mn ratios; (a) Mn-3, (b) undoped, (c) K-2, and (d) K-3. Current density is 20 mA g^{-1}.

monoclinic phase (JCPDS: 42-1317) was observed [8]. Therefore, it was found that the stacking phases were modified by the addition of potassium nitrate as the starting materials.

Fig. 14 shows the discharge–recharge curves of the synthesized products of Mn-3, undoped, K-2, and K-3 samples. All the birnessite samples in Figs. 14(b–d) that underwent galvanostatic cycling had S-shaped curves and the discharge reaction occurred around 3 V. The discharge capacity of Mn-3 is much lower than that of the undoped sample. The decrease in the discharge capacity is due to the formation of the high crystalline hollandite phase [22] because the K ion in the tunnel prevents diffusion of the Li ion. The initial discharge capacities of K-3 and K-2 are similar to that of the undoped sample.

Fig. 15 shows the plots of the discharge capacities vs. cycle number for Mn-3, undoped, K-2, and K-3 samples. In this figure, the synthesized products of the undoped, K-2, and K-3 indicate analogous maximum discharge capacities of about 170 mAh g^{-1} at the 2nd cycle. However, these capacity retentions are different during 20 cycles. The discharge capacities of the K-3, K-2, undoped, and Mn-3 products at the 20th cycle are 145, 133, 96, and 41 mAh g^{-1}, respectively. The capacity retentions, the discharge ratio between the 2nd and the 20th cycles, of K-3, −2, and undoped samples are about 85, 80, and 56%, respectively. The synthesized products with excess potassium additives exhibited an improvement in the capacity retention. However, the discharge capacities of the K-5 and K-10 (not shown here) were similar to that of undoped sample during cycling, that is, the electrode performances of the monoclinic stacking phase are not improved. The Mn-3 has a lower discharge capacity with capacity fading. Therefore, we recognized that the enhancement of the capacity retention depends on the stacking structure, i.e., increase of the 3R stacking phase and decrease of the 2H stacking phase. It is believed that the effect of cobalt doping and 3R phase plays an important role on the cycling behavior. The lamellar manganese dioxides for a lithium secondary battery application would provide an improvement in the high rechargeable capacity and satisfactory cycle performance by designing nano structures including the stacking sequence resulted from the modification of calcination conditions.

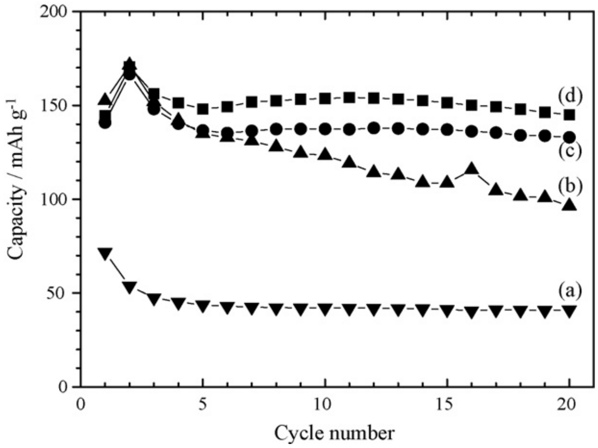

Fig. 15. Variation in discharge capacities of synthesized samples with various mole ratios of K/Mn; (a) Mn-3, (b) undoped, (c) K-2, and (d) K-3.

4. Conclusion

The potassium birnessites doped with Co, Ni, or Al were successfully obtained from $KMnO_4$ mixed with these nitrates by a calcination synthesis. Among the doped compounds, Co-25 birnessite has the highest discharge capacity of 200 mAh g^{-1} and capacity retention of about 80% for 20 cycles. It was found that the electrochemical performance of birnessite doped with appropriate amount of cobalt was improved due to the change in the stacking structure and the decrease in the charge transfer resistance. Furthermore, the initial discharge capacity of the synthesized birnessite by excess K additives was comparable to the undoped birnessite, and the capacity retention of the synthesized birnessite with excess K additives is higher than the undoped one. The difference in the electrochemical performance was ascribed to the structure change, as confirmed by XRD, AAS, XPS, and Raman measurements.

Acknowledgements

The authors thank Dr. T. Sasaki and Mr. K. Saka for their helpful assistance in the experimental work. This study was partially supported by the New Energy and Industrial Technology Development Organization (NEDO), Japan, Yazaki Memorial Foundation for Science and Technology, and Iwatani Naoji Foundation's Research Grant.

References

[1] T. Ohzuku, M. Kitagawa, T. Hirai, J. Electrochem. Soc. 137 (1990) 769.
[2] S.-T. Myung, S. Komaba, K. Kurihara, N. Kumagai, Solid State Ionics 177 (2006) 733.
[3] M.M. Doeff, A. Anapolsky, L. Edman, T.J. Richardson, L.C. De Jonghe, J. Electrochem. Soc. 148 (2001) A230.
[4] S.H. Kim, S.J. Kim, A.M. Oh, Chem. Mater. 11 (1999) 557.
[5] S.H. Kim, W.M. Im, J.K. Hong, A.M. Oh, J. Electrochem. Soc. 147 (2000) 413.
[6] A.-C. Gaillot, D. Flot, V.A. Drits, A. Manceau, M. Burghammer, B. Lanson, Chem. Mater. 15 (2003) 4666.
[7] A.-C. Gaillot, V.A. Drits, A. Plancon, B. Lanson, Chem. Mater. 16 (2004) (1890).
[8] A.-C. Gaillot, B. Lanson, V.A. Drits, Chem. Mater. 17 (2005) 2959.
[9] A. Ogata, S. Komaba, N. Kumagai, Electrochemistry 74 (2006) 28.
[10] S. Komaba, N. Kumagai, S. Chiba, Electrochim. Acta 46 (2001) 31.
[11] H. Peters, K.H. Radeke, L.Z. Till, Anorg. Allg. Chem. 346 (1966) 1.
[12] H.Y. Lee, V. Manivannan, J.B. Goodenough, C. R. Acad. Sci., Ser. IIc: Chim. 2 (1999) 565.
[13] M. Tsuda, H. Arai, Y. Sakurai, J. Power Sources 110 (2002) 52.
[14] C. Julien, M. Massot, R. Baddour-Hadjean, S. Franger, S. Bach, J.-P. Pereira-Ramos, Solid State Ionics 159 (2003) 345.
[15] S. Franger, S. Bach, J. Farcy, J.-P. Pereira-Ramos, N. Baffier, J. Power Sources 109 (2002) 262.
[16] R. Chen, P. Zavalij, M.S. Whittingham, Chem. Mater. 8 (1996) 1275.
[17] R. Chen, M.S. Whittingham, J. Electrochem. Soc. 144 (1997) L64.
[18] S. Komaba, T. Sasaki, N. Kumagai, Electrochem. Acta 50 (2005) 2297.
[19] J.F. Moulder, W.F. Stickle, P.E. Sobol, K.D. Bomben, in: J. Chastain (Ed.), Handbook of X-ray Photoelectron Spectroscopy, PerkinElmer, 1992.
[20] C. Julien, M. Massot, Phys. Chem. Chem. Phys. 4 (2002) 4226.
[21] P.K. Sharma, G.J. Moore, F. Zhang, P. Zavalij, M.S. Whittingham, Electrochem. Solid-State Lett. 2 (1999) 494.
[22] T. Sasaki, N. Kumagai, S. Komaba, H. Yashiro, Electrochemistry 72 (2004) 688.